



Cite this: *RSC Adv.*, 2020, **10**, 39562

# Selective formation of pyridinic-type nitrogen-doped graphene and its application in lithium-ion battery anodes†

Jacob D. Bagley,<sup>a</sup> Deepan Kishore Kumar,<sup>b</sup> Kimberly A. See <sup>a</sup> and Nai-Chang Yeh <sup>\*c</sup>

We report a high-yield single-step method for synthesizing nitrogen-doped graphene nanostripes (N-GNSPs) with an unprecedentedly high percentage of pyridinic-type doping (>86% of the nitrogen sites), and investigate the performance of the resulting N-GNSPs as a lithium-ion battery (LIB) anode material. The as-grown N-GNSPs are compared with undoped GNSPs using scanning electron microscopy (SEM), Raman spectroscopy, X-ray photoelectron spectroscopy (XPS), helium ion-beam microscopy (HIM), and electrochemical methods. As an anode material we find that pyridinic-type N-GNSPs perform similarly to undoped GNSPs, suggesting that pyridinic sites alone are not responsible for the enhanced performance of nitrogen-doped graphene observed in previous studies, which contradicts common conjectures. In addition, post-mortem XPS measurements of nitrogen-doped graphene cycled as a lithium-ion battery anode are conducted for the first time, which reveal direct evidence for irreversible chemical changes at the nitrogen sites during cycling. These findings therefore provide new insights into the mechanistic models of doped graphene as LIB anodes, which are important in improving the anode designs for better LIB performance.

Received 16th July 2020  
Accepted 19th October 2020

DOI: 10.1039/d0ra06199a

rsc.li/rsc-advances

## 1. Introduction

Increasing the energy density of lithium-ion batteries (LIBs) is an important issue in energy research in order to meet growing energy demands and long-term sustainability.<sup>1</sup> The energy density of LIBs depends on the charge storage capacities and potentials of the battery electrode materials. Therefore, one approach to improve LIB energy density is to increase the capacity of the anode, *i.e.*, the amount of lithium that the anode can reversibly accommodate. The current industry standard LIB anode material is graphite, and the processing of graphite for LIBs has been developed to the point that its practical performance is approaching its theoretical capacity.<sup>2,3</sup> Therefore, new materials are being explored to develop next-generation high energy density LIB anodes.<sup>3</sup> Among them, doping graphene with heteroatoms (*e.g.*, nitrogen, boron, *etc.*) as the anode material is an appealing approach because doped graphene LIB anodes have demonstrated reversible capacities greater than

1000 mA h g<sup>−1</sup> (167% higher than graphite) with good lifetimes (>500 cycles).<sup>4–10</sup> Additionally, doped graphene is chemically similar to graphite so that it is compatible with current LIB assemblies (*e.g.*, electrolyte compatibility).

Although doped graphene anodes have demonstrated good performance, the effects of dopant type and dopant configuration on LIB performance is not well understood. This gap in knowledge is in part due to the difficulty in preparing graphene with a single dopant type in a specific configuration, such that measurements to date generally involve convoluted effects from multiple dopants and/or different dopant configurations.

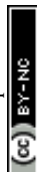
Nitrogen is the most studied graphene dopant, and nitrogen can substitute into the graphene lattice in three different configurations that are termed as graphitic, pyrrolic, and pyridinic, as illustrated in Fig. 1.<sup>11,12</sup> At the graphitic sites, nitrogen bonds to three carbon atoms and preserves the graphene honeycomb lattice. At the pyrrolic sites, nitrogen is adjacent to a vacancy defect and bonds to two carbons that are part of a five-membered ring. At the pyridinic sites, nitrogen is adjacent to a vacancy defect and bonds to two carbons that are part of a six-membered ring. In addition to their structural characteristics, these sites differ electronically so that the specific sites can be identified and quantified by X-ray photoelectron spectroscopy (XPS).<sup>11</sup> Among different types of nitrogen-doped graphene sites, the pyridinic type has been conjectured to yield the highest lithium storage capacity based on empirical results, although LIB applications of nitrogen-doped graphene with

<sup>a</sup>Division of Chemistry and Chemical Engineering, California Institute of Technology, Pasadena, CA, 91125, USA

<sup>b</sup>Department of Electrical Engineering, California Institute of Technology, Pasadena, CA, 91125, USA

<sup>c</sup>Department of Physics, California Institute of Technology, Pasadena, CA, 91125, USA. E-mail: ncyeh@caltech.edu

† Electronic supplementary information (ESI) available. See DOI: 10.1039/d0ra06199a



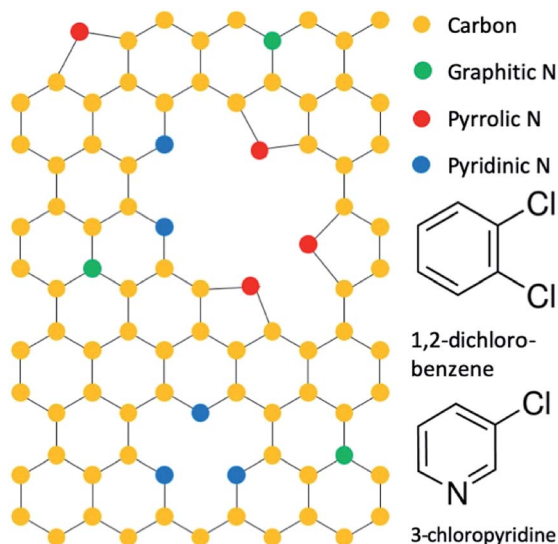


Fig. 1 Configuration of nitrogen dopants in graphene and precursor molecules 1,2-dichlorobenzene and 3-chloropyridine.

purely pyridinic-sites has never been accomplished so that the conjecture cannot be directly verified.<sup>10–14</sup> Thus, the purpose of this work is to examine the validity of current conjectures by studying the performance of nitrogen-doped graphene nanomaterials with predominant pyridinic-type doping in a LIB anode configuration.

Herein, we report the synthesis of nitrogen-doped graphene nanostripes (N-GNSPs) with predominantly pyridinic sites and the application of such N-GNSPs as the anode material in LIBs. In addition, we report for the first time post-mortem XPS characterization that reveals direct evidences for chemical changes at the nitrogen doped sites during the LIB operation. Although our N-GNSPs have a similar nitrogen content (~8%) as other reports and an unprecedentedly high percentage of pyridinic content (>86% of the nitrogen sites), these materials only demonstrate limited enhancement (~13%) in gravimetric lithium storage capacity when compared to undoped graphene nanostripes (GNSPs). We also observe irreversible chemical changes at the nitrogen sites *via* XPS during solid electrolyte interphase (SEI) formation, *i.e.*, the electronically insulating and Li<sup>+</sup>-conducting interface that forms on LIB electrodes due to solvent decomposition during the first cycle. These findings therefore imply that pyridinic sites alone are unlikely responsible for the enhanced performance of nitrogen-doped graphene observed in previous studies, and further investigations are necessary to understand the effects of nitrogen doping on the performance of LIB anodes.

## 2. Experimental

### 2.1 Synthesis of graphene materials

N-GNSPs were synthesized by modifying the plasma enhanced chemical vapour deposition (PECVD) synthesis for GNSPs that was previously presented by Hsu *et al.*<sup>15</sup> Specifically, a microwave induced hydrogen/methane plasma with traces 1,2-

dichlorobenzene (Alfa Aesar, 99%) or 3-chloropyridine (Alfa Aesar, 99%) yielded GNSPs or N-GNSPs on Cu-substrates, respectively. The PECVD growth system was custom built and consisted of eight parallel deposition chambers. Each chamber included a 0.75 cm × 1.25 cm copper foil (McMaster-Carr, 99.9%) in a “1/2” outer diameter glass tube fitted with an Evenson cavity (Ophos Instruments Inc., Frederick, MD, USA) excited by a 2.45 GHz microwave power source (ENS 4 × 200 W CPS, SAIREM, Décines-Charpieu, France). All chambers simultaneously received 70 W of microwave power, which created a plasma volume of ~1 cm<sup>3</sup>. H<sub>2</sub> (99.999%) and CH<sub>4</sub> (99.999%) gases were introduced to the chamber by mass flow controllers (MC series, Alicat Scientific, Tuscon, AZ, USA), and traces of 1,2-dichlorobenzene (3-chloropyridine) were introduced to the chamber *via* a leak valve from a vacuum sealed vial of 1,2-dichlorobenzene (3-chloropyridine). The pressure in the chamber before splitting into eight chambers was held at 3.8 Torr, the total flow rates of H<sub>2</sub> and CH<sub>4</sub> were 48 sccm and 5 sccm, respectively, and the ratio of CH<sub>4</sub> to 1,2-dichlorobenzene (3-chloropyridine) was ~2 : 1 as measured by a residual gas analyser (RGA; XT300M, Extorr Inc., New Kensington, PA, USA) placed upstream of the deposition chamber and connected *via* a capillary, as detailed in ESI Note 1 and schematically shown in Fig. S1.† The plasma was maintained for ~3 hours to synthesize sufficient graphene material for use as LIB anodes. We note that the synthesis yield was found to be linear with the growth time at a rate of ~6 mg cm<sup>-2</sup> hour per chamber on copper substrates, as described in ESI Note 2 and demonstrated in Fig. S2.† For each LIB electrode slurry (described in Section 2.3), we used 100–150 mg graphene. By employing all eight PECVD chambers in parallel for graphene growth, we were able to collect sufficient material in ~3 hours to make an electrode slurry which could make anodes for several coin cells.

### 2.2 Characterization of fabricated graphene materials

Raman spectroscopy was performed in a Renishaw M-1000 Micro-Raman (Renishaw, Gloucestershire, UK) spectrometer operating with a 514.5 nm argon ion laser with a spectral resolution of 1 cm<sup>-1</sup> and a spot size of ~20 μm. A dual-wedge polarization scrambler was inserted to depolarize the laser. Scanning electron microscopy (SEM) was performed in a Hitachi S-4100 (Hitachi, Tokyo, Japan) with an accelerating voltage of 5 kV. Helium-ion beam microscopy (HIM) imaging was performed in a ZEISS ORION NanoFab (Pleasanton, CA, USA) with an accelerating voltage of 30 kV, a beam current of 1.2 pA and a working distance of 8.021 mm. XPS data were collected using a Kratos AXIS Ultra spectrometer (Kratos Analytical, Manchester, UK). The instrument was equipped with a hybrid magnetic and electrostatic electron lens system, a delay-line detector and a monochromatic Al Kα X-ray source (1486.7 eV). Data were collected at a pressure of ~5 × 10<sup>-9</sup> Torr with photoelectrons collected at 0° with respect to the sample. For the survey spectra the analyser pass energy was 80 eV and the step size was 1 eV, and for all other spectra the analyser pass energy was 10 eV and the step size was 0.025 eV. The instrument energy scale and work function were calibrated using clean Au,



Ag and Cu standards. The instrument was operated by Vision Manager software v. 2.2.10 revision 5. The data were analysed using CasaXPS software (CASA Software Ltd). The carbon  $sp^2$  peaks were fit as asymmetric Gaussian–Lorentzian, and all other peaks were fit as symmetric Gaussian–Lorentzian. In addition, the carbon  $sp^3$  and  $\pi-\pi^*$  satellite peaks were constrained to be 0.8 eV and 6.4 eV higher binding energy than the  $sp^2$  peak, respectively. For post mortem XPS characterizations the data were boxcar averaged using a width of eleven points to improve the signal-to-noise ratio.

### 2.3 Coin cell preparation

Working electrodes, which consisted of graphene material (GNSP or N-GNSP), carbon black (Super-P, Alfa Aesar, >99%) and polyvinylidene fluoride (PVDF, MTI corporation, >99.5%) binder in a 7:2:1 ratio, were mixed in *N*-methyl-2-pyrrolidinone (NMP, Sigma-Aldrich, 99.5%) in a centrifugal mixer (AR-100 Thinky USA, Inc., Laguna Hills, CA, USA) at 5000 rpm for 10 minutes. The resulting slurry was spread across copper foil (McMaster-Carr, 99.9%) using a doctor blade with a thickness of “0.2” and dried at 120 °C in vacuum for 16 hours “~7/16” diameter circular electrodes were cut from the dried slurry/copper foil. Separately, as-deposited N-GNSPs on the copper growth substrate were used as working electrodes. Two-electrode 2032 coin cells (MTI) were assembled in an argon filled glove box (with  $O_2 < 0.1$  ppm and  $H_2O < 0.1$  ppm). The counter/reference electrodes were lithium foil (Sigma Aldrich, 99.9%, 0.75 mm, mechanically cleaned immediately before cell assembly), and the electrolyte was 1 M LiPF<sub>6</sub> (Sigma Aldrich, ≥99.99%) in ethylene carbonate/dimethyl carbonate (1:1 mixture by volume, both Sigma Aldrich, ≥99%). Dimethyl carbonate was stored over molecular sieves (3 Å, Beantown Chemical) prior to use, and the electrolyte was mixed in a dried HDPE bottle. A polypropylene separator (Celgard 2400) was used and ~8 drops of electrolyte were used in each coin cell. Details of the coin cell fabrication procedure are given in ESI Note 3 and schematically shown in Fig. S3.† After electrochemical cycling, coin cells were disassembled in an argon filled glovebox, and the working electrodes were rinsed with dimethyl carbonate and transferred in an argon filled container directly to the XPS ultrahigh vacuum chamber for post mortem XPS characterization.

### 2.4 Electrochemical characterization

All electrochemical measurements were performed on a reference 600 (Gamry Instruments, Warminster, PA, USA). Galvanostatic charge–discharge measurements were taken at indicated current densities within a voltage range of 3 V to 0.01 V.

## 3. Results and discussion

### 3.1 Pyridinic N-GNSP synthesis rationale and comparison to previous syntheses

We accomplished synthesis of predominantly pyridinic type N-GNSPs by modifying precursors used in our previous

synthesis of undoped GNSPs.<sup>15</sup> In the original synthesis, trace content of 1,2-dichlorobenzene (structure shown in Fig. 1) in a hydrogen/methane plasma resulted in growth of high quality (in terms of the chemical purity and crystallinity) vertically oriented graphene on a copper substrate. We note that vertically oriented graphene refers to a class of graphene nanomaterials wherein graphene grows vertically with respect to the growth substrate forming wall-like nanostructures on the substrate.<sup>16</sup> We believe that in the synthesis of GNSPs, 1,2-dichlorobenzene forms benzene radicals in the plasma due to the weak C–Cl bonds, which then seed and propagate the graphene structure along with methane radicals assisting the growth and hydrogen radicals etching away defects. The role of methane and hydrogen was proposed by other researchers studying the growth of vertically oriented graphene,<sup>16</sup> and the role of 1,2-dichlorobenzene is corroborated by our previous findings of the RGA data showing substantial increase in C<sub>6</sub> and C<sub>6</sub>H<sub>6</sub> during the growth of GNSPs in the presence of 1,2-dichlorobenzene.<sup>15</sup> For the synthesis of pyridinic type N-GNSPs, we replace 1,2-dichlorobenzene with 3-chloropyridine (see Fig. 1). Similarly, we conjecture that 3-chloropyridine yields pyridine radicals in the plasma due to the weak C–Cl bond, which then seed the N-GNSP structures. We further conjecture that the use of 3-chloropyridine for graphene growth yields predominantly pyridinic-type N-GNSPs (see Section 3.2) because the bonding configuration of nitrogen in 3-chloropyridine resembles the bonding configuration of nitrogen in pyridinic graphene sites.

As demonstrated in Section 3.2, we find that this method indeed produces N-GNSPs that are >86% pyridinic-type doping for the nitrogen-doped sites. To the best of our knowledge, this is the highest fraction of pyridinic-type doping that has been accomplished with high yield and good crystallinity. For comparison, we briefly summarize here previous reports of related studies: Bang *et al.*,<sup>17</sup> Mombeshora *et al.*,<sup>18</sup> and Yasuda *et al.*<sup>19</sup> reported selective synthesis of pyridinic type nitrogen-doped graphene. However, the Raman peaks of each of these materials were relatively wide, indicating structural disorder.<sup>20</sup> Yang *et al.* reported a synthesis of nitrogen-doped graphene with fairly narrow Raman peaks, but the pyridinic doping content was only ~50%.<sup>21</sup> Wisitsoraat *et al.* reported a nitrogen-doped graphene synthesis with narrow Raman peaks, but the doping type was completely pyrrolic.<sup>22</sup> Finally, Luo *et al.*<sup>23</sup> reported a selective synthesis of pyridinic type nitrogen-doped graphene with narrow Raman peaks, but the material was monolayer graphene, and thus the yield was insufficient for applications in LIB.

### 3.2 Characterization of the as-grown material

Graphene nanomaterials fabricated by the aforementioned PECVD methods were characterized by SEM, helium-ion beam microscopy (HIM), Raman spectroscopy, XPS and electrochemical methods. Normal incidence SEM images of as grown GNSPs and N-GNSPs are shown in Fig. 2A and B, respectively. The top edge of the vertical graphene sheets are visible as bright lines in the images. Pores between vertical graphene sheets are



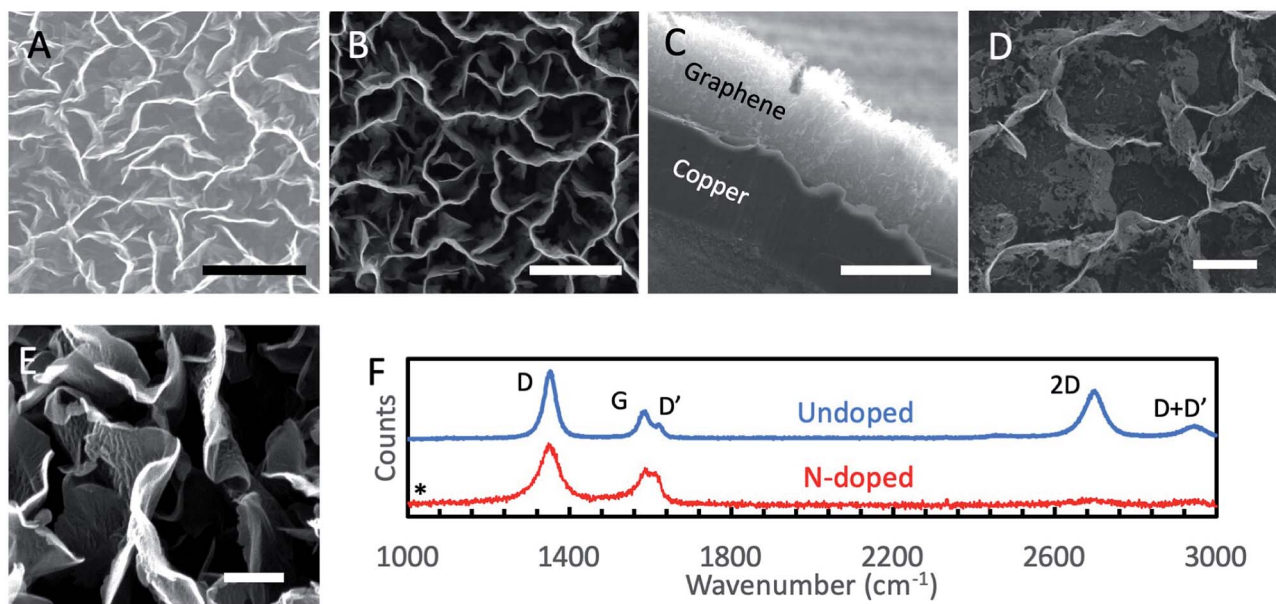


Fig. 2 (A) Normal incidence SEM image of the as-grown GNSPs. Scale bar: 2  $\mu\text{m}$ . (B) Normal incidence SEM image of the as-grown N-GNSPs. Scale bar: 2  $\mu\text{m}$ . (C) Cross sectional SEM image of the as-grown N-GNSPs. Scale bar: 20  $\mu\text{m}$ . (D) Normal incidence HIM image of the as-grown GNSPs, showing perforations at the edges, which we conjecture to result from the vacancies associated with the pyridinic sites. Scale bar: 1  $\mu\text{m}$ . (E) Normal incidence HIM image of the as-grown GNSPs, showing no perforations at the edges. Scale bar: 200 nm. (F) Raman spectra of the undoped GNSPs and N-GNSPs, showing significantly suppressed 2D-band in N-GNSPs, which may be attributed to the substantial presence of vacancies due to N-doping. The absence of a peak at  $1034\text{ cm}^{-1}$  (marked by an asterisk) demonstrates residual 3-chloropyridine is not present on the sample.

darker in the image because electrons cannot escape to the detector from the deep pores. Sheets that do not stand perfectly vertical are visible as medium contrast points in the image. Visually, the GNSPs and N-GNSPs are structurally similar, *i.e.*, they have similar pore and sheet sizes. A cross sectional image is shown in Fig. 2C, where the height of the vertical graphene nanomaterial measures at  $\sim 20\text{ }\mu\text{m}$ . To further differentiate the microscopic structures of GNSPs and N-GNSPs, we employed HIM imaging, which can resolve features as small as  $\sim 3\text{ nm}$  without damaging graphene under correct experimental conditions.<sup>24</sup> Fig. 2D displays a HIM image of N-GNSPs which reveals perforations in the N-GNSPs sheets, whereas Fig. 2E does not show perforations in the GNSPs sheets. Further, previous transmission element microscopy studies on GNSPs do not reveal perforations in GNSPs sheets.<sup>15</sup> We conjecture that pyridinic sites are present at the edges of the perforations, and the perforations are the result of vacancies associated with the pyridinic sites.

The Raman spectrum (Fig. 2F) of GNSPs and N-GNSPs nanomaterials confirms the growth of graphene with the characteristic D ( $1361\text{ cm}^{-1}$ ), G ( $1589\text{ cm}^{-1}$ ) and 2D ( $2704\text{ cm}^{-1}$ ) peaks.<sup>25</sup> These materials also exhibit the D' ( $1609\text{ cm}^{-1}$ ) and D + D' ( $2945\text{ cm}^{-1}$ ) peaks which together with the G and D' peaks being well resolved classify the samples as nanocrystalline graphene material according to the three stage defect model.<sup>20,25</sup> We acknowledge that the D-peak is very intense in these graphene samples, which is in part due to the abundant edges.<sup>15</sup>

Comparing the GNSP and N-GNSP spectra, we find that the intensity ratios and the full-width-half-maximum (FWHM) of

the D and G peaks are similar, whereas the 2D peak is much suppressed in N-GNSPs relative to the undoped GNSPs, which is consistent with previous observation of N-doped graphene materials and may be attributed to the presence of vacancies associated with the N-doped sites.<sup>11,26</sup> The absence of residual 3-chloropyridine on the sample is confirmed by the absence of a peak in the Raman spectrum at  $1034\text{ cm}^{-1}$  (marked by an asterisk), which is the position of a very strong 3-chloropyridine Raman signal.<sup>27</sup>

We conducted XPS studies to quantitatively determine the chemical composition and doping type in our materials (see Table 1 for a compositional analysis of the N-GNSPs). The survey spectrum of the undoped GNSP material (Fig. 3A) shows a pure carbon material. The C-1s spectrum of the same undoped GNSP material (Fig. 3B) was fit with three peaks corresponding to  $\text{sp}^2$  hybridized C-C bonds ( $284.9\text{ eV}$ ),  $\text{sp}^3$  hybridized C-C bonds ( $285.7\text{ eV}$ ), and a  $\pi-\pi^*$  satellite ( $291.4\text{ eV}$ ). The strong  $\text{sp}^2$  peak and the presence of the  $\pi-\pi^*$  peak verify the graphene crystallinity, *i.e.*, domains with delocalized p-orbitals.<sup>28,29</sup> The N-GNSP survey spectrum (Fig. 3C) shows the material is composed of 89.4% carbon, 7.5% nitrogen and 3.1% chlorine. Notably, there is no oxygen peak in our N-GNSPs (even though the sample was exposed to air), which is in contrast to the typical presence of oxygen in other doped graphene materials made at scales appropriate for LIB application.<sup>4-10</sup>

The C-1s high resolution spectrum of N-GNSPs (Fig. 3D) is analysed by considering five components that correspond to  $\text{sp}^2$  hybridized C-C bonds ( $284.9\text{ eV}$ ),  $\text{sp}^3$  hybridized C-C bonds ( $285.7\text{ eV}$ ), C-N bonds ( $285.8\text{ eV}$ ), C-Cl bonds ( $287.1\text{ eV}$ ), and

**Table 1** Compositional analysis of the N-GNSP material from XPS fitting. (Slight discrepancies between fractions and sums are due to rounding)

Element	Configuration	Peak position (eV)	Concentration (%)	Fraction of total composition (%)
C	$sp^2$	289.4	89.4	24.0
	$sp^3$	285.7		30.6
	C–N	285.8		16.6
	C–Cl	287.1		3.1
	$\pi$ – $\pi^*$	291.9		17.8
N	Pyridinic	399.5	7.5	6.5
	Pyrrolic	401.5		1.0
Cl	C–Cl	202.5/200.9	3.1	2.8
	C–Cl <sub>x</sub>	197.8/196.7		0.4

a  $\pi$ – $\pi^*$  satellite (291.9 eV). The C–C bonds and the satellite peak assignments are justified by the literature (*i.e.*, the peak positions and relative spacings are consistent with previous reports),<sup>30</sup> and the C–Cl and C–N peak assignments are justified by comparing the relative peak intensities of carbon, nitrogen and chlorine components (Table 1). We acknowledge here that the  $sp^3$ -hybridized C-component in the N-GNSP sample is relatively large (30.6% of total composition), which initially seems incongruent with our claim of having a graphene nanomaterial, which should have consisted of purely  $sp^2$ -hybridized C. However, noting that XPS is a surface sensitive technique,<sup>31</sup> we attribute the measured  $sp^3$  signals to the edge structure of the GNSPs and N-GNSPs exposed due to the vertical growth, *i.e.*, the  $sp^3$  signal is artificially high because the edges are more exposed than the basal plane. Additionally, the N-GNSPs sample likely has a larger  $sp^3$  component due to more  $sp^3$  defects in the sample, as evidenced by a slightly wider D peak and larger D' peak in the Raman spectrum.

For the N-1s high resolution spectrum, we followed previously reported assignments and fit the data to a superposition of two peaks that corresponded to contributions from the pyridinic sites (399.5 eV) and pyrrolic sites (401.5 eV).<sup>11</sup> We found that the pyridinic sites accounted for ~86% of the nitrogen content. This is an unprecedentedly large ratio of pyridinic type nitrogen doping sites, particularly considering the relatively narrow Raman peaks (Fig. 2F) and a relatively high yield. In the case of the Cl-2p high resolution spectrum (Fig. 3F), we considered the contributions of two components (with four peaks due to the  $2p_{1/2}/2p_{3/2}$  splitting), which corresponded to C–Cl bonds (201.9/200.3 eV) and C–Cl<sub>x</sub> bonds (197.2/196.1 eV).<sup>32</sup>

### 3.3 Electrochemical characterization

The fabricated graphene nanomaterials (both GNSPs and N-GNSPs) were tested for LIB anode application *via* galvanostatic charging/discharging (Fig. 4A–C) and rate performance analysis (Fig. 4D) by assembling with conductive additive and

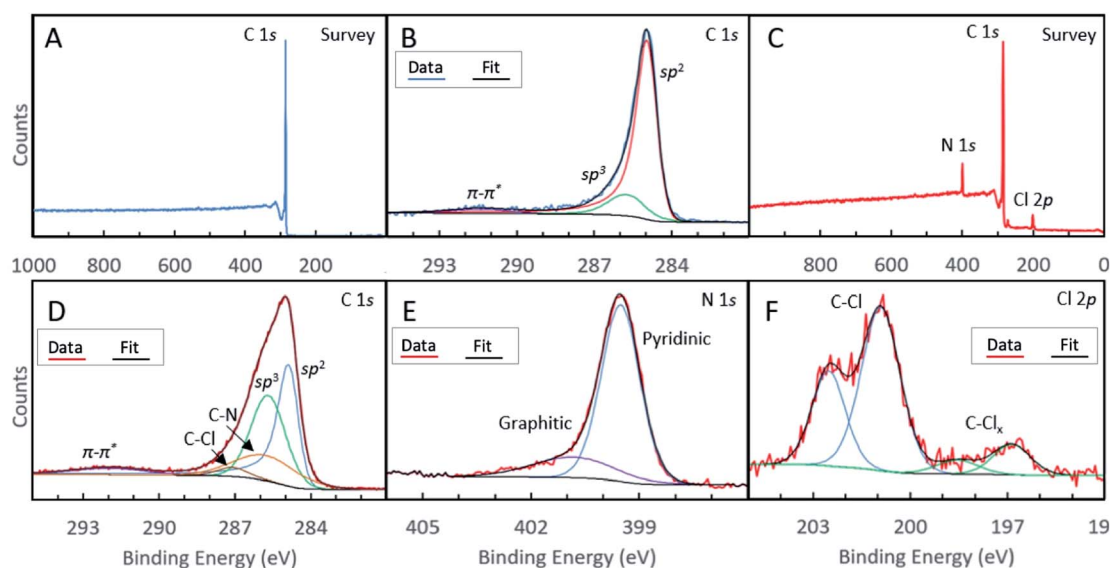


**Fig. 3** (A) XPS survey spectrum of undoped GNSPs, showing a pure carbon composition. (B) XPS high resolution C-1s spectrum of GNSPs. (C) XPS survey spectrum of N-GNSPs, showing 89.4% carbon, 7.5% nitrogen and 3.1% chlorine. High resolution XPS spectra of N-GNSPs for (D) C-1s (E) N-1s and (F) Cl-2p.



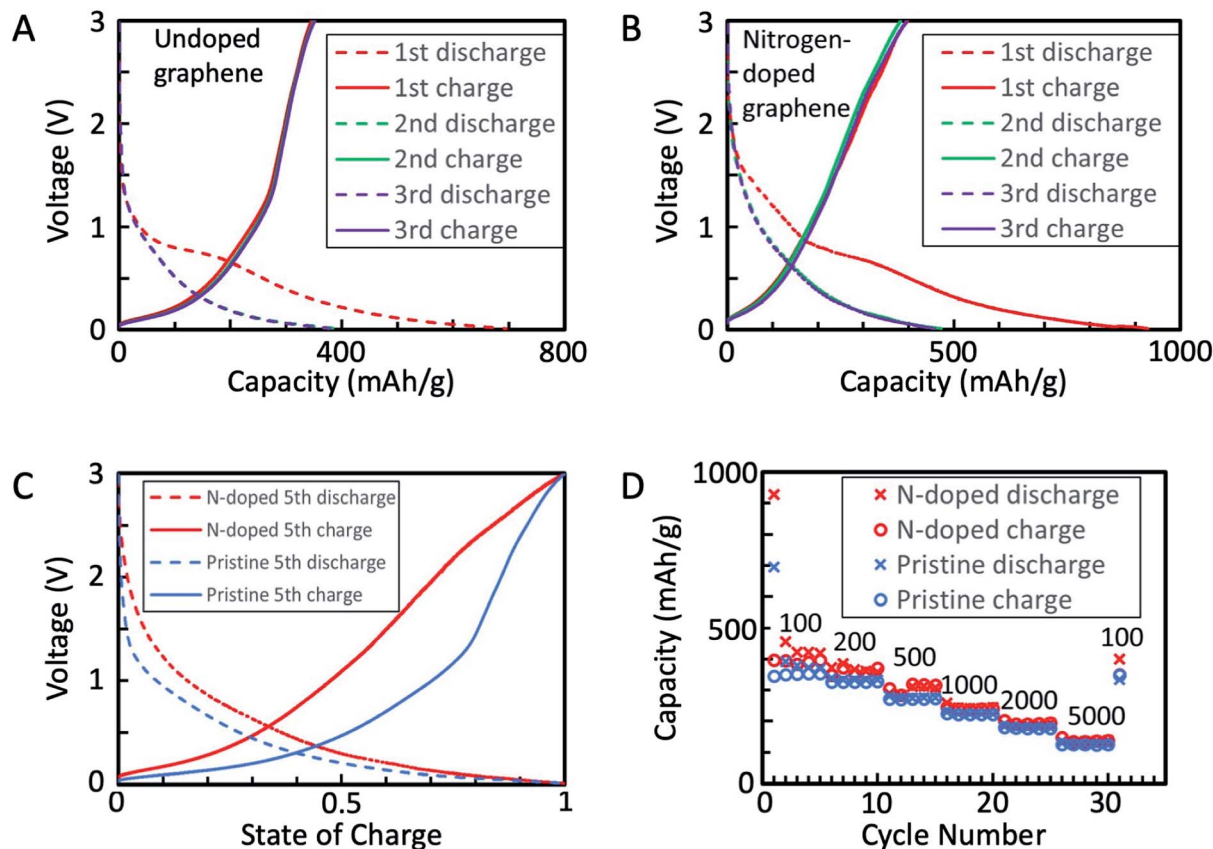


Fig. 4 (A) First three cycles of galvanostatic charge/discharge for GNSP anode. Rate: 100 mA g<sup>-1</sup>. Note: the second discharge is eclipsed by the third discharge. (B) First three cycles of galvanostatic charge/discharge for N-GNSP anode. Rate: 100 mA g<sup>-1</sup>. Note: the second discharge is eclipsed by the third discharge. (C) Galvanostatic charge/discharge of the fifth cycle of both the GNSP and N-GNSP anodes normalized by state of charge. Rate: 100 mA g<sup>-1</sup>. (D) Rate performance of GNSPs and N-GNSPs with the rate of each cycle (in mA g<sup>-1</sup>) indicated above the data. All voltages are referenced to Li/Li<sup>+</sup>.

polymer binder in a coin cell configuration. These data resemble previously reported graphene LIB anode data in that the discharge capacity substantially decreased between the first and second cycles, the redox potentials varied substantially with the state of charge, and the capacity decreased with increasing charge/discharge rates.<sup>4–10</sup> For both GNSPs and N-GNSPs, SEI formation during the first cycle was apparent as a plateau at 800–700 mV, consistent with the report in literature.<sup>33</sup> After the first discharge, the charge/discharge curves (Fig. 4A and B) nearly completely overlapped, indicating that the SEI entirely forms during the first discharge. The reversible capacities of the GNSP and N-GNSP anodes at 100 mA g<sup>-1</sup> are ~373 mA h g<sup>-1</sup> and ~423 mA h g<sup>-1</sup>, respectively (Fig. 4A and B), and both anodes returned to these values after cycling at high rates, suggesting minimal capacity fade (Fig. 4D). At 100 mA g<sup>-1</sup> the capacity of N-GNSPs was 13% higher than the capacity of GNSPs; the implications of this observation will be discussed in Section 4. To compare the voltage profiles of the GNSP and N-GNSP anodes, we plotted in Fig. 4C the voltage as a function of anode state-of-charge (SOC). Both the charge and discharge profiles of N-GNSPs showed a higher redox potential than the undoped GNSPs for all SOC, suggesting that the pyridinic nitrogen had beneficial effects on the reduction kinetics and detrimental effects to the oxidation kinetics.

Additionally, to compare the electrochemically active surface areas of GNSPs and N-GNSPs, we estimated the double layer capacitance (which is linearly proportional to the active surface area) based on the galvanostatic charge/discharge curves, as detailed in ESI Note 4 and Fig. S4.† The estimated double layer capacitance of GNSPs and N-GNSPs is 5.6 F g<sup>-1</sup> and 10.8 F g<sup>-1</sup>, respectively, suggesting that N-GNSPs have a significantly higher surface area than GNSPs per unit mass, which is consistent with the perforations of N-GNSPs as imaged in Fig. 2D. While the double layer capacitance for the N-GNSPs electrode is nearly twice of the capacitance of the undoped GNSPs electrode, the lithium storage capacitance of the N-GNSPs electrode is only 14% higher than the GNSPs electrode. This discrepancy suggests that although the double layer capacitance and the lithium storage capacitance follow the same trend between these two materials, they are not necessarily related. That is, the lithium storage capacitance is due to faradaic charge storage rather than non-faradaic charge storage.

### 3.4 Post mortem XPS characterization of N-GNSP LIB anodes

To study the chemical changes that occur at dopant sites during the LIB operation, we performed XPS characterization on N-GNSP anodes after lithium cycling. For these experiments,

samples were prepared without polymer binders and conductive additives to simplify data interpretation and to avoid contamination from polymers of the XPS ultrahigh vacuum environment. Rather, because our N-GNSP material grew directly on a copper foil, the as-grown sample with its copper substrate was assembled directly into a coin cell, as shown in the right panel of Fig. S3.† Three samples were prepared this way, each with an open-circuit voltage of  $\sim 3$  V vs. Li/Li<sup>+</sup>, and each sample was subjected to different conditions. The first, labelled “rest”, was kept at open circuit for  $\sim 3$  days. The second, labelled “800 mV”, was cycled between 3 V (open-circuit voltage) and 800 mV five times, leaving the cell charged at 3 V. The third, labelled “10 mV”, was cycled between 3 V (open-circuit voltage) and 10 mV five times, leaving the cell charged at 3 V. Coin cells were cycled five times to ensure the relevant chemical processes proceeded to completion. Then, each coin cell was de-primed in an argon-filled glovebox, rinsed with dimethyl carbonate, and dried in a vacuum chamber without being exposed to air. The samples were subsequently transferred to an argon-filled air-tight suitcase directly to the XPS load lock chamber. In addition, the top layers of sample “10 mV” were removed by gently scraping the sample with a spatula in the glovebox to reduce interference from the SEI. In addition, because these samples were very porous (see Fig. 2B), the electrolyte salt was not effectively removed from the surface even after rinsing the samples with dimethyl carbonate. The resulting XPS spectra displayed a strong signal from the salt and a weak (and noisy) signal from the graphene material. Therefore, we smoothed the data using boxcar averaging with a width of eleven points. This width was justified as the step size was 0.025 eV, so a width of eleven points was 0.25 eV, which was much smaller than the

width of the XPS peaks (see Fig. 5). For completeness, we provide the raw data for Fig. 5 in Fig. S5.†

XPS analysis of these samples revealed that the nitrogen sites (Fig. 5A) became chemically altered during cycling. We attribute the peak at  $\sim 402.1$  eV to lithiation of the nitrogen sites (*e.g.*, N-Li<sup>+</sup>) and the peak at 404.4 eV to solvent decomposition that resulted in either oxygen functionalization (N-O) or carbonation (N-CO<sub>2</sub>-R) of the nitrogen sites. These assignments may be justified as follows. Given the composition of the battery cell contents, the only possible chemical functionalization would involve carbon, lithium, oxygen, phosphorus, and fluorine. We can rule out phosphorus and fluorine functionalization because the N-1s binding energies for N-P and N-F bonds were reported in the range 397.3 eV to 400.3 eV and 417.1 eV, respectively, according to the XPS database of National Institute of Standards and Technology (NIST),<sup>34</sup> which differed from our measured peak positions. Therefore, the peak shifts after lithium cycling were likely due to lithiation and carbon/oxygen interactions. We assign N-Li<sup>+</sup> (lithiation) and N-O/N-CO<sub>2</sub>-R (solvent decomposition) to the peaks at 402.1 eV and 404.4 eV, respectively, because solvent decomposition reactions on nitrogen sites likely occurred during the SEI formation (which was, in fact, solvent and salt decomposition<sup>33</sup>), but the solvent decomposition peak could only appear after the electrode was cycled to potentials beyond the SEI formation potential.

The chlorine 2p peak also shifted in the samples assembled into battery cells after lithium cycling (Fig. 5B). However, the peak shifted to a lower binding energy and becomes convoluted with the phosphorus 2s peak, the latter resulted from the LiPF<sub>6</sub> salt physisorbed to the surface. Therefore, detailed analysis of the chlorine 2p peak was difficult, although it is reasonable to

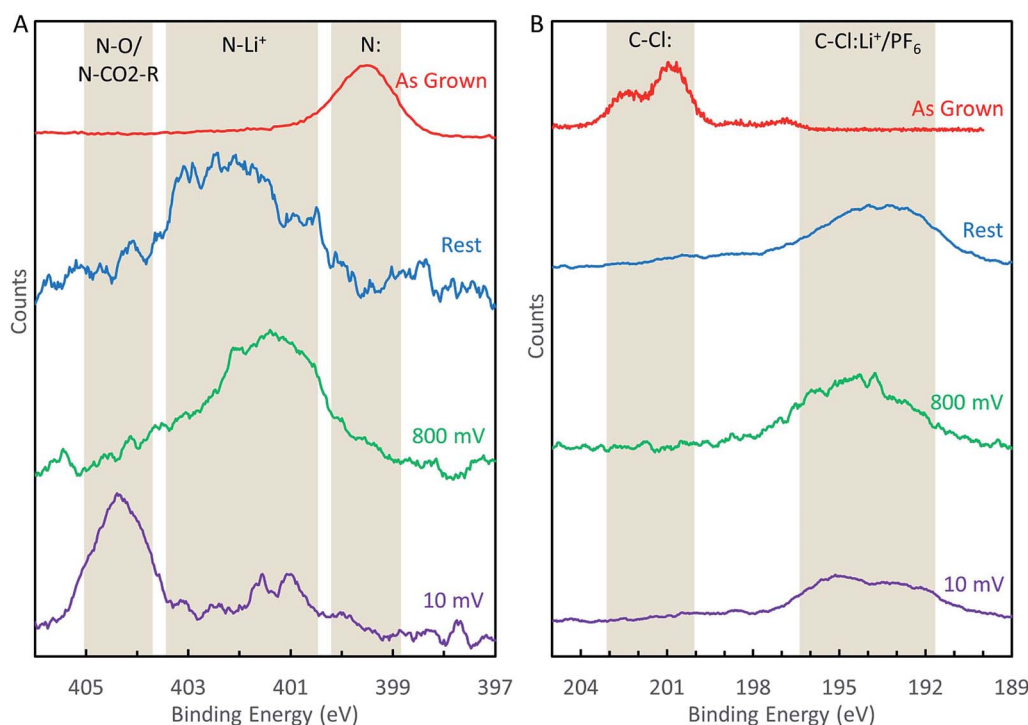


Fig. 5 (A) Evolution of the N-1s XPS peak during LIB cycling. (B) Evolution of the Cl-2p XPS peak during LIB cycling.



**Table 2** Brief comparison of reported reversible capacities, doping and Raman spectra profiles of several studies of graphene LIB anodes. Values in blue are estimated from figures in references cited

Study	% nitrogen (% pyridinic)	Other dopants	Raman spectra peaks FWHM (cm <sup>-1</sup> )	Surface area (m <sup>2</sup> g <sup>-1</sup> )	Reversible capacity (mA h g <sup>-1</sup> )	Reference
1	1.5 (33)	15% S 14% O 1% H	D peak: 130 G peak: 140	624	1110	4
2	1.8 (25)	6% S 5.2% O	D and G peaks are convoluted	906	3525	9
3	2 (57)	O <sup>a</sup>	D peak: 80 G peak: 70	<sup>a</sup>	900	10
4	3.1 (65)	3.1% O	D peak: 110 G peak: 80	290	500	6
5	0 (0)	1.8% P 3.25% O	D peak: 100 G peak: 70	<sup>a</sup>	450	7
6	7.5 (87)	3.1% Cl	D peak: 65 G peak: 76		423	This work

<sup>a</sup> Authors did not specify the amount.

assign the peak to Cl–Li<sup>+</sup> bond,<sup>34</sup> and some forms of solvent decomposition also cannot be ruled out.

Given the aforementioned peak assignments, we may describe the evolution of the nitrogen sites during the LIB charging/discharging cycles as follows. Even in the absence of any applied bias, nitrogen sites will bind Li<sup>+</sup> once assembled in a battery, as illustrated by the “rest” spectrum in Fig. 5A. This N–Li<sup>+</sup> interaction persists when the battery is cycled between 3 V and 0.8 V, as shown by the “800 mV” spectrum in Fig. 5A. If the battery is cycled below 800 mV, nitrogen sites become irreversibly functionalized due to solvent decomposition, as demonstrated by the “10 mV” spectrum in Fig. 5A. We believe that these findings can serve as useful input for computation studies of LIB anode reaction mechanisms, which have not yet considered different chemical shifts of electrode components under different reactions.<sup>14</sup>

## 4. Discussion

Our experimental results suggest that selectively pyridinic-type nitrogen-doped graphene nanomaterials do not significantly increase the capacity of graphene nanomaterials. We also suggest that this lack of capacity enhancement is not due to the chlorine dopants as chlorine doping has also been demonstrated to increase the capacity of graphene nanomaterials, *i.e.*, chlorine does not have a deleterious effect on lithium storage capacity.<sup>8</sup> To understand the origin of improved LIB performance previously reported for pyridinic-type nitrogen-doped graphene materials, we provide in Table 2 a brief summary of the characterization and performance of doped graphitic materials reported in several studies.

For instance, the material used in study 1 of Table 2 has fairly broad D and G peaks in the Raman spectra, contains significant amounts of other dopants, has a large surface area and demonstrates a moderately high reversible capacity of ~1000 mA h g<sup>-1</sup>. Study 2 reports a colossally high reversible capacity of 3525 mA h g<sup>-1</sup>, and the nitrogen-doped graphene in

this study displays a Raman spectrum with D and G peaks so broad that they overlap (suggesting strong disorder), has a large surface area, and contains additional sulfur and oxygen dopants. On the other hand, the materials in studies 4 and 5 demonstrate smaller reversible capacities and display moderately broad peaks in the Raman spectra, smaller surface areas and fewer dopants than the materials in studies 1, 2 and 3. Our work (study 6 in Table 2) displays the narrowest Raman peaks, purest nitrogen-doping, and the smallest reversible capacity.

While the comparison in Table 2 is by no means exhaustive, it reveals a trend that better performing doped graphene materials generally contain significant crystalline disorder (as demonstrated by the broad peaks in their Raman spectra) and have larger surface areas. Additionally, graphene materials containing multiple dopants appear to perform better, although this trend cannot be well established based on limited comparison in Table 2. On the other hand, researchers have recently substantiated that incorporating multiple dopants in graphene nanomaterials can improve the electrocatalytic effect through the synergism among different heteroatoms or nitrogen sites.<sup>35–37</sup> Such synergetic effects may also take place in the case of LIB applications, although there are insufficient experimental data to draw this conclusion at present.

The phenomenon of high capacity in disordered carbon materials has been studied for decades, and several models have been proposed to explain it (*e.g.*, see Section 2.3.3 in ref. 38). While many recent studies have focused on incorporating dopants to enhance lithium storage, it is possible that the dopants themselves have little effect on the lithium storage capacity. Rather, structural disorder that is coincident with doping may be the essential factor affecting the lithium storage capacity.

## 5. Conclusion

We have demonstrated a novel method of synthesizing nitrogen-doped graphene nanostripes with an unprecedentedly



high percentage of pyridinic-type doping (>86% of the nitrogen sites) and good crystallinity, performed studies of such selectively pyridinic type nitrogen-doped graphene as LIB anode materials, and provided experimental evidences for changes in the chemical state of nitrogen sites during LIB operation for the first time *via* XPS studies as a function of the cycling voltage. Our findings reveal that pyridinic-type nitrogen-doping alone does not significantly enhance the LIB anode performance when compared to an undoped graphene sample, suggesting that pyridinic sites may not be responsible for the enhanced performance of nitrogen-doped graphene materials observed in previous studies. We hypothesize that strong crystalline disorder, high surface area and possibly multiple types of dopants in the LIB anode material may be important to increasing the reversible capacity. Additionally, post mortem XPS characterization of the N-GNSP LIB anodes further reveals immediate lithiation of the nitrogen sites upon contact with lithium electrolyte and functionalization of nitrogen sites by solvent decomposition and coincident SEI formation. These findings thus provide useful insights into more intelligent design and mechanistic understanding of doped graphene anodes for better LIB performance.

## Author contributions

J. D. Bagley developed the 8-chamber PECVD growth system, synthesized N-GNSPs, carried out Raman spectroscopic characterization, SEM surface characterization, XPS studies, and fabrications of LIB anodes and coin cells. D. Kishore Kumar carried out the HIM measurement and synthesized GNSPs. K. See contributed to the LIB studies and provided the facilities for the coin cell fabrications. N.-C. Yeh coordinated the research project and data analysis, and wrote the manuscript together with J. D. Bagley.

## Conflicts of interest

There are no conflicts to declare.

## Acknowledgements

This research was jointly supported by the United Advanced Materials and the National Science Foundation under the Institute for Quantum Information and Matter (IQIM) at Caltech (Award #1733907). We thank Professor George R. Rossman for allowing our access to his Raman spectroscopic facilities, and also acknowledge the use of XPS/UPS at the Beckman Institute and HIM at the Kavli Nanoscience Institute at Caltech.

## Notes and references

- 1 J. Hong, S. Park and N. Chang, Accurate remaining range estimation for electric vehicles, *21st Asia and South Pacific Design Automation Conference (ASP-DAC)*, IEEE, Macau, China, 2016.
- 2 M. Ko, S. Chae, J. Ma, N. Kim, H.-W. Lee, Y. Cui and J. Cho, Scalable synthesis of silicon-nanolayer-embedded graphite

- for high-energy lithium-ion batteries, *Nat. Energy*, 2016, **1**, 16113.
- 3 J. W. Choi and D. Aurbach, Promise and reality of post-lithium-ion batteries with high energy densities, *Nat. Rev. Mater.*, 2016, **1**, 16013.
- 4 H. Shan, X. Li, Y. Cui, D. Xiong, B. Yan, D. Li, A. Lushington and X. Sun, Sulfur/nitrogen dual-doped porous graphene aerogels enhancing anode performance of lithium ion batteries, *Electrochim. Acta*, 2016, **205**, 188–197.
- 5 Z. Xing, Z. Ju, Y. Zhao, J. Wan, Y. Zhu, Y. Qiang and Y. Qian, One-pot hydrothermal synthesis of Nitrogen-doped graphene as high-performance anode materials for lithium ion batteries, *Sci. Rep.*, 2016, **6**, 26146.
- 6 Z.-S. Wu, W. Ren, L. Xu, F. Li and H.-M. Cheng, Doped graphene sheets as anode materials with superhigh rate and large capacity for lithium ion batteries, *ACS Nano*, 2011, **5**, 5463–5471.
- 7 C. Zhang, N. Mahmood, H. Yin, F. Liu and Y. Hou, Synthesis of phosphorus-doped graphene and its multifunctional applications for oxygen reduction reaction and lithium ion batteries, *Adv. Mater.*, 2013, **25**, 4932–4937.
- 8 J. Xu, I.-Y. Jeon, J.-M. Seo, S. Dou, L. Dai and J.-B. Baek, Edge-selectively halogenated graphene nanoplatelets (XGnPs, X = Cl, Br, or I) prepared by ball-milling and used as anode materials for lithium-ion batteries, *Adv. Mater.*, 2014, **26**, 7317–7323.
- 9 X. Ma, G. Ning, Y. Sun, Y. Pu and J. Gao, High capacity Li storage in sulfur and nitrogen dual-doped graphene networks, *Carbon*, 2014, **79**, 310–320.
- 10 H. Wang, C. Zhang, Z. Liu, L. Wang, P. Han, H. Xu, K. Zhang, S. Dong, J. Yao and G. Cui, Nitrogen-doped graphene nanosheets with excellent lithium storage properties, *J. Mater. Chem.*, 2011, **21**, 5430–5434.
- 11 H. Wang, T. Maiyalagan and X. Wang, Review on recent progress in nitrogen-doped graphene: synthesis, characterization, and its potential applications, *ACS Catal.*, 2012, **2**, 781–794.
- 12 Y. Shao, S. Zhang, M. H. Engelhard, G. Li, G. Shao, Y. Wang, J. Liu, I. A. Aksay and Y. Lin, Nitrogen-doped graphene and its electrochemical applications, *J. Mater. Chem.*, 2010, **20**, 7491–7496.
- 13 A. L. M. Reddy, A. Srivastava, S. R. Gowda, H. Gullapalli, M. Dubey and P. M. Ajayan, Synthesis of nitrogen-doped graphene films for lithium battery application, *ACS Nano*, 2010, **4**, 6337–6342.
- 14 C. Ma, X. Shao and D. Cao, Nitrogen-doped graphene nanosheets as anode materials for lithium ion batteries: a first-principles study, *J. Mater. Chem.*, 2012, **22**, 8911–8915.
- 15 C.-C. Hsu, J. D. Bagley, M. L. Teague, W.-S. Tseng, K. L. Yang, Y. Zhang, Y. Li, Y. Li, J. M. Tour and N.-C. Yeh, High-yield single-step catalytic growth of graphene nanostripes by plasma enhanced chemical vapor deposition, *Carbon*, 2018, **129**, 527–536.
- 16 Z. Bo, Y. Yang, J. Chen, K. Yu, J. Yan and K. Cen, Plasma-enhanced chemical vapor deposition synthesis of vertically oriented graphene nanosheets, *Nanoscale*, 2013, **5**, 5180–5204.



- 17 G. S. Bang, G. W. Shim, G. H. Shin, D. Y. Jung, H. Park, W. G. Hong, J. Choi, J. Lee and S.-Y. Choi, Pyridinic-N-Doped Graphene Paper from Perforated Graphene Oxide for Efficient Oxygen Reduction, *ACS Omega*, 2018, **3**, 5522–5530.
- 18 E. T. Mombeshora, P. G. Ndungu and V. O. Nyamori, The physicochemical properties and capacitive functionality of pyrrolic- and pyridinic-nitrogen, and boron-doped reduced graphene oxide, *Electrochim. Acta*, 2017, **258**, 467–476.
- 19 S. Yasuda, L. Yu, J. Kim and K. Murakoshi, Selective nitrogen doping in graphene for oxygen reduction reactions, *Chem. Commun.*, 2013, **49**, 9627–9629.
- 20 A. C. Ferrari and D. M. Basko, Raman spectroscopy as a versatile tool for studying the properties of graphene, *Nat. Nanotechnol.*, 2013, **8**, 235–246.
- 21 S.-Y. Yang, K.-H. Chang, Y.-L. Huang, Y.-F. Lee, H.-W. Tien, S.-M. Li, Y.-H. Lee, C.-H. Liu, C.-C. M. Ma and C.-C. Hu, A powerful approach to fabricate nitrogen-doped graphene sheets with high specific surface area, *Electrochem. Commun.*, 2012, **14**, 39–42.
- 22 A. Wisitsoraat, D. Phokaratkul, T. Maturos, K. Jaruwangrangsee and A. Tuantranont, Synthesis and characterization of nitrogen-doped 3D graphene foam prepared by inductively-coupled plasma-assisted chemical vapor deposition, *IEEE 15 Int. Conf. on Nanotechnology*, IEEE, Rome, Italy, 2015.
- 23 Z. Luo, S. Lim, Z. Tian, J. Shang, L. Lai, B. MacDonald, C. Fu, Z. Shen, T. Yu and J. Lin, Pyridinic N doped graphene: synthesis, electronic structure, and electrocatalytic property, *J. Mater. Chem.*, 2011, **31**, 8038.
- 24 D. Fox, Y. B. Zhou, A. O'Neill, S. Kumar, J. J. Wang, J. N. Coleman, G. S. Duesberg, J. F. Donegan and H. Z. Zhang, Helium ion microscopy of graphene: beam damage, image quality and edge contrast, *Nanotechnol.*, 2013, **24**, 335702.
- 25 A. C. Ferrari and J. Robertson, Interpretation of Raman spectra of disordered and amorphous carbon, *Phys. Rev. B: Condens. Matter Mater. Phys.*, 2000, **61**, 14095–14107.
- 26 A. Das, S. Pisana, B. Chakraborty, S. Piscanec, S. K. Saha, U. V. Waghmare, K. S. Novoselov, H. R. Krishnamurthy, A. K. Geim, A. C. Ferrari and A. K. Sood, Monitoring dopants by Raman scattering in an electrochemically top-gated graphene transistor, *Nat. Nanotechnol.*, 2008, **3**, 210–215.
- 27 J. H. S. Green, W. Kynaston and H. M. Paisley, Vibrational spectra of monosubstituted pyridines, *Spectrochim. Acta*, 1963, **19**, 549–564.
- 28 H. Darmstadt and C. Roy, Surface spectroscopic study of basic sites on carbon blacks, *Carbon*, 2003, **41**, 2662–2665.
- 29 R. Blume, D. Rosenthal, J.-P. Tessonier, H. Li, A. Knop-Gericke and R. Schlögl, Characterizing graphitic carbon with X-ray photoelectron spectroscopy: a step-by-step approach, *ChemCatChem*, 2015, **7**, 2871–2881.
- 30 S. T. Jackson and R. G. Nuzzo, Determining hybridization differences for amorphous carbon from the XPS C-1s envelope, *Appl. Surf. Sci.*, 1995, **90**, 195–203.
- 31 S. Tanuma, C. J. Powell and D. R. Penn, Calculations of electron inelastic mean free paths. II. Data for 27 elements over the 50–2000 eV range, *Surf. Interface Anal.*, 1991, **17**, 911–926.
- 32 E. Papirer, R. Lacroix, J.-B. Donnet, G. Nansé and P. Fioux, XPS study of the halogenation of carbon black—Part 2. Chlorination, *Carbon*, 1995, **33**, 63–72.
- 33 P. Verma, P. Maire and P. Novák, A review of the features and analyses of the solid electrolyte interphase in Li-ion batteries, *Electrochim. Acta*, 2010, **55**, 6332–6341.
- 34 NIST X-ray photoelectron spectroscopy database, <https://srdata.nist.gov/xps/>, accessed June 2020.
- 35 H. Fu, K. Huang, G. Yang, Y. Cao, H. Wang, F. Peng, Q. Wang and H. Yu, Synergistic Effect of Nitrogen Dopants on Carbon Nanotubes on the Catalytic Selective Oxidation of Styrene, *ACS Catal.*, 2020, **10**, 129–137.
- 36 X. Ning, Y. Li, J. Ming, Q. Wang, H. Wang, Y. Cao, F. Peng, Y. Yang and H. Yu, Electronic synergism of pyridinic- and graphitic-nitrogen on N-doped carbons for the oxygen reduction reaction, *Chem. Sci.*, 2019, **10**, 1589–1596.
- 37 F. Dong, Y. Cai, C. Liu, J. Liu and J. Qiao, Heteroatom (B, N and P) doped porous graphene foams for efficient oxygen reduction reaction electrocatalysts, *Int. J. Hydrogen Energy*, 2018, **43**, 12661–12670.
- 38 M. Winter, J. O. Besenhard, M. E. Spahr and P. Novák, Insertion Electrode Materials for Rechargeable Lithium Batteries, *Adv. Mater.*, 1998, **10**, 725–763.

